Environmental Pollution 340 (2024) 122788

Contents lists available at ScienceDirect

Environmental Pollution

journal homepage: www.elsevier.com/locate/envpol

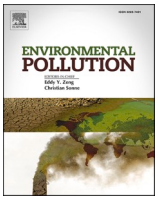

Sustainable gliadin - Metal oxide composites for efficient inactivation of *Escherichia coli* and remediation of cobalt (II) from water☆

Emile Salomon Massima Mouele [a,b,*], John Kwame Bediako [a,c,**], Youssef El Ouardi [a], Ikenna Anugwom [a], Svetlana Butylina [a], Jean-Luc Mukaba [b], Leslie F. Petrik [b], Myo Tay Zar Myint [d], Htet Htet Kyaw [e], Mohammed Al-Abri [e], Mohammed A. Al Belushi [f], Sergey Dobretsov [f], Katri Laatikainen [a], Eveliina Repo [a]

[a] Department of Separation Science, School of Engineering Science, Lappeenranta-Lahti University of Technology (LUT), FI-53850, Lappeenranta, Finland
[b] Environmental and Nano Sciences Group, Department of Chemistry, University of the Western Cape, Bellville, 7535, South Africa
[c] Department of Food Process Engineering, School of Engineering Sciences, College of Basic and Applied Sciences, University of Ghana, P. O. Box LG 77, Legon, Accra, Ghana
[d] Department of Physics, College of Science, Sultan Qaboos University, P. O. Box 36, 123 Al-Khoud, Muscat, 123, Oman
[e] Nanotechnology Research Center, Sultan Qaboos University, P. O. Box 33, Al-Khoud, Muscat, 123, Oman
[f] Central Laboratory for Food Safety, Food Safety and Quality Center, Ministry of Agriculture, Fisheries Wealth & Water Resources, PO Box 3094, Airport Central Post, 111, Muscat, Oman

ARTICLE INFO

Keywords:
MOs-gliadin composites
Multifunctionality
Antibacterial
Toxic *E. coli*
Adsorption capacity
Water purification

ABSTRACT

Bio-based materials facilitate greener approach to engineering novel materials with multifunctional properties for various applications including water treatment. In this study, we extracted gliadin from wheat gluten using alcoholic solvent. The aggregation limitations of gliadin protein were overcome by functionalisation with metal oxides (MOs) TiO_2, $AgFe_2O_3$ and $AgFe–TiO_2$ prepared by chemical precipitations. The novel composites were characterised by scanning electron microscopy-energy dispersive X-ray spectroscopy (SEM-EDS), Fourier-transform infrared spectroscopy (FTIR), X-Ray diffraction (XRD), thermogravimetry analysis (TGA), Brunauer Emmet–Teller (BET), and zeta potential. The multifunctionality of MOs-gliadin composites was tested through toxic *Escherichia coli* (*E. coli)* inactivation and Co^{2+} adsorption from water. The antibacterial results showed excellent inhibition under both dark and light conditions. The maximum Co^{2+} uptake, 101 mg/g was reached with TiO_2@gliadin after 24 h and best fitted the Langmuir isotherm model. The adsorption process followed pseudo-second order model with an equilibrium adsorption capacity, $q_{e2} = 89.86$ mg/g closer to the experimental data. Thermodynamic investigations indicated that $\Delta G^{\circ} = -9.677$ kJ/mol, $\Delta H^{\circ} = -123$ kJ/mol, and $\Delta S^{\circ} = 0.490$ J.K/mol, respectively, suggesting that adsorption was spontaneous and endothermic. The regenerated TiO_2@gliadin composite was still efficient after five consecutive cycles. This study demonstrates that MOs-gliadin blended composites are sustainable for water purification.

1. Introduction

Cobalt occurs naturally and is mostly found in soil, water, rocks, plants, and animals, including humans with diverse applications in products, such as pigments, metal alloys, and batteries (Atsdr Agency for Toxic Substances and Disease Registry, 2023). Cobalt is an indispensable element for living organisms, its presence in vitamin B12 favours the production of red blood cells (The National Institute for Occupational Safety and Health (NIOSH), 2019; Health Encyclopedia, 2023; Czarnek et al., 2015). Nevertheless, prolonged exposure to cobalt may cause

☆ This paper has been recommended for acceptance by Sarah Harmon.

* Corresponding author. Department of Separation Science, School of Engineering Science, Lappeenranta-Lahti University of Technology (LUT), FI-53850, Lappeenranta, Finland.

** Corresponding author. Department of Separation Science, School of Engineering Science, Lappeenranta-Lahti University of Technology (LUT), FI-53850, Lappeenranta, Finland.

E-mail addresses: emilemassima@yahoo.fr (E.S. Massima Mouele), john.bediako@lut.fi (J.K. Bediako).

https://doi.org/10.1016/j.envpol.2023.122788
Received 14 June 2023; Received in revised form 5 September 2023; Accepted 21 October 2023
Available online 23 October 2023

severe effects on blood, lungs, skin, and even result in toxic cardiomyopathy and cancer (The National Institute for Occupational Safety and Health (NIOSH), 2019; Health Encyclopedia, 2023) (Czarnek et al., 2015). Due to these acute effects, the utmost concentration of Co^{2+} in drinking water approved by the World Health Organization (WHO) should be around 4 x10^{-5} g L^{-1} (Jing et al., 2019).

Conversely, the presence of bacteria such as *Escherichia coli* (*E. coli*) in potable water may affect humans (Odonkor and Mahami, 2020). *E. coli* is frequently found in warm-blooded animals including humans (World Health Organization et al., 2018). Most *E. coli* strains are innocuous, however, some strains such as verotoxigenic *E. coli* (VTEC) and Shiga toxin-producing *E. coli* (STEC) can be sources of various diseases (World Health Organization et al., 2018). *E. coli* can be transmitted through faecal contamination of water and food, or cross-contamination during food preparation (Kostyla et al., 2015). The ingestion of small amounts of *E. coli*, and exposure to potential source such as contaminated water can result in an infection called *E. coli* O157 or VTEC (Diseases & Conditions and Coli, 2022). The immediate symptoms include abdominal pain, diarrhoea, vomiting, and kidney failure (Kostyla et al., 2015; Diseases & Conditions and Coli, 2022). The occurrence of *E. coli* in water is indicative of faecal contamination and possible pathogenic exposure (Washington State Department of Health, 2023). Therefore, it is crucial to treat *E. coli* contaminated water before direct or indirect uses.

The development of adequate methods for the extraction of Co^{2+} from aqueous solutions together with bacterial inactivation are of global interest. Many studies have been conducted on the use of various adsorbents to remove Co^{2+} from aqueous systems with outstanding adsorption capacities as reported in various publications (Awual et al., 2014; Awual et al., 2015; Awual et al., 2017). However, the problematic use of toxic chemicals in the production of adsorbents often limits their applicability, especially considering the growing emphasis on environmental sustainability. The use of protein complexes in the manufacturing of novel proteinic composites is a promising research approach. The occurrences of amino groups in proteins' chemical structures offer them the ability to coordinate/link with bioactive elements and other chemical species (Abaee et al., 2017a). Nano-sized proteins possess exceptional functional properties including, biodegradability, biocompatibility, surface activity, amphiphilic nature, film-forming ability, water binding capacity, gelation, etc. (Verma et al., 2018; Lohcharoenkal et al., 2014; Abaee et al., 2017b). These features have been widely explored in food research while their application in chemical oxidation and adsorption have gained is scant attention. Though previous investigations reported wide application of proteinic compounds (PCs) in the delivery of specific drugs into living systems (Zimet and Livney, 2009; Sneharani et al., 2010; Somchue et al., 2009), the utilization of protein composites for the immobilization of toxic metals from aqueous mixtures is limited. Indeed, the processability of bioproteins (BPs) for environmental remediation is often challenging because of their chemical phenomena such as swelling and aggregations making them unattractive (Liao et al., 2016a). For instance, Yang et al. (2018) recalled that gliadin nanoparticles displayed minimal trapping efficacy and were often characterised by aggregation tendency. Oleyaei et al. (2016) and Mallakpour and Barati (2011) proposed that these limitations could be overcome by engineering composite materials containing nanoparticles. Nanomaterials derived from various transition metals and their oxides such as silver, titanium dioxide, iron, etc. have found application in chemical oxidation and adsorption (Sayed and Polshettiwar, 2015; Amendola et al., 2015; Sahoo and Gupta, 2015; Majidi et al., 2016; Nishida et al., 2017; Üstün et al., 2022; Kleinfeldt et al., 2019). Therefore, their incorporation together with protein structures yield new materials with advanced surface area, and suitable functional groups that may result in better adsorption capacity. This classifies BPs as potential host matrices that can accommodate diverse chemical entities to promote their physical and chemical characteristics (Filipcsei et al., 2007; Tyagi et al., 2020; Sapna, 2018; Borjigin et al., 2022). Metal oxides (MOs) fillers have an adequate specific surface area and high surface energy, thus could be used in protein complexation to significantly boost the composites' mechanical, thermal, and barrier properties. Titanium dioxide (TiO_2) with diverse attributes including nontoxicity, low cost, odourless, antibacterial, and excellent photocatalytic activity has been broadly used in this regard. It is recognised that an adequate dosage of TiO_2 into protein matrices is a crucial approach to improve their physicochemical properties (Wang et al., 2012; Zolfi et al., 2014). However, the blending of PCs such as gliadin with doped TiO_2 or co-doped with transition metals (TMs) has not been extensively explored thus far. Gliadin is a hydrophobic protein resulting from wheat gluten and is mostly soluble in alcoholic solvents (Wu et al., 2018a). The chemical coordination of amino groups in the gliadin molecule is responsible for its supreme hydrophobicity that is noticeable in alkaline pH (Thewissen et al., 2011). It is assumed that gliadin can link to noxious metals through electrostatic interactions and hydrogen bonding. However, during storage, gliadin nanoparticles easily aggregate and exhibit low trapping efficacy which could be alleviated by blending with co-doped TiO_2-MOs. This may improve its physicochemical stability resulting in a sustainable multifunctional composite. Therefore, in this study, tuneable amounts of TiO_2, $AgFe_2O_3$, or AgFe–TiO_2 were combined gliadin to manufacture novel proteinic composites with improved physicochemical, thermal, and functional properties that were then applied as adsorbents for simultaneous remediation of Co^{2+} and *E. coli* as representative pollutants from water.

2. Materials

The preparation of gliadin blended composites reported in this paper was performed using various chemicals including iron (II) sulphate hexahydrate ($FeSO_4.6H_2O$), sodium hydroxide (NaOH) pellets, and absolute ethanol (AnalaR Normapur) procured from "Besloten Vennootschap met Beperkte Aansprakelijkheid" (BVBA), Belgium. Silver nitrate ($AgNO_3.6H_2O$) puriss and titanium tetraisopropoxide (TTIP) were acquired from Kebo Lab (member of Merk group, Switzerland), and Urea (Reagent plus R $\geq$ 99.5 % pallet) from Sigma Aldrich, USA. Gluten from wheat was obtained from Sigma Aldrich, Australia.

2.1. Methods

2.1.1. Extraction of gliadin from wheat gluten and preparation of MO-gliadin composites

20 g of wheat gluten was dissolved in 200 mL of 70 % ethanol at a ratio of 1:10 (w: v) and stirred at (400 rpm) for 2 h at 70 °C. The solution was allowed to cool down to room temperature. Glutenin was separated from gliadin eluent by centrifugation at 5000 rpm for 10 min. The ethanol content in the gliadin extract was evaporated by rotavapor @ 40 °C, and the resultant solution was portioned into P_1 and P_2. The P_1 gliadin solution was frozen in a cool environment (-4 to 4 °C) for 48 h and freeze-dried for further characterization. The preparation and freeze drying of gliadin-metal oxide (v:v ratio 1:1) composites were conducted following procedures in the supplementary materials, text S1 and text S2.

2.1.2. Characterisation of gliadin blend composites

The morphological properties of gliadin blended composites were examined with a Hitachi SU3500 scanning electron microscope (SEM) at an acceleration voltage of 15 kV, and sample images were recorded at various magnifications. The elemental composition and mapping micrographs of the specimens were acquired by energy dispersive X-ray spectroscopy (EDS) attached to SEM using Pathfinder software. The functional group properties of the as-prepared gliadin blend composites were studied by Fourier-transform infrared spectroscopy connected to an attenuated reflectance mode (FT/ATR) in the range of 4000 to 300 cm^{-1} using a PerkinElmer FT-IR Spectrometer Frontier 207. The X-Ray diffraction (XRD) measurement of gliadin blended composites was

performed using a multipurpose D8-Advance X-ray diffractometer (Bruker D8, Germany) in the angular range of 10°–90°, with Cu–K radiation at a wavelength of 1.5406 Å, at 40 kV and 40 mA. The thermal decomposition of gliadin blend composites was studied by thermogravimetry analysis (TGA) using a TGA/DTA, STA 449C/4/Jupiter® thermal analyser (NETZSCH-Geratebau GmbH, Selb, Germany). The TGA investigation was achieved by heating 10 mg of the specimen in DTA/TG crucible (Al_2O_3) within a linear temperature range of 25–900 °C, heating rate 10 °C/min; under nitrogen (N_2) gas at a flow rate of 40 mL/min. The nitrogen adsorption/desorption isotherms used to examine the specific surface area of gliadin composites were studied by Brunauer Emmet–Teller (BET) analysis that was conducted using Micro metrics 3 Flex equipment. The electrical stability of the gliadin blend composites in aqueous media was investigated by means of a Zetasizer Nano ZS (Malvern Instruments).

2.1.3. Antimicrobial bioassay and adsorption studies

The antibacterial activity of gliadin blended composites was tested on the inhibition of Gram-negative *E. coli* and the experimental protocols are detailed in S3.

The adsorption investigations for the removal of Co^{2+} by gliadin blended composites are expressed in Equations. (1 and 2).

$$R(\%) = ((C\_i - C\_e) / C\_i) \times 100 \quad (1)$$

$$q\_e = ((C\_i - C\_e) / m) \times V \quad (2)$$

Where $R(\%)$ *is the* removal efficiency and q_e (mg/g or mmol/g) the adsorption capacity at equilibrium, C_i and C_e (mg/L) are the initial and equilibrium concentrations of Cobalt, m (g) is the mass of the pollutant, and V (L) is the solution volume, correspondingly.

The adsorption isotherms were fitted using the Langmuir (Equation (3)), Freundlich (Equation (4)) and Temkin (Equation (5)) models detailed in supplementary data S5 – S7.

$$q_e = \frac{q_m K_L C_e}{1 + K_L C_e} \quad (3)$$

$$q_e = K_F C_e^{n_F} \quad (4)$$

$$q_e = \frac{RT}{b_T} \ln(A_T C_e) \quad (5)$$

where K_L (L/mmol) is the affinity constant, K_F (mmol/g (L/mmol) ^{nF})) and n_F are Freundlich adsorption constants, while $RT/b_T = B_T$ (J/mol) and A_T (L/mmol) are the heat of adsorption, and the equilibrium binding constant, respectively.

The adsorption kinetic studies were evaluated using pseudo-first order (PS1) (Equations (6) and (7)), pseudo-second order (PS2) (Equations (8) and (9)) and intraparticle diffusion (Equation (10)) models detailed in the supplementary data, S8 – S11. Where k_1 is the PS1 rate constant (min $^{-1}$) and k_2 the pseudo-second-order rate constant (g/mmol min), k_d (mmol/gmin$^{1/2}$) is the rate constant of intraparticle diffusion and C (mg/g) the thickness of the boundary layer, and t is the equilibrium time, respectively.

$$\frac{dq}{dt} = k_1(q_e - q) \quad (6)$$

$$\ln(q_e - q_t) = \ln q_e - k_1 t \quad (7)$$

$$\frac{dq}{dt} = k_2(q_e - q)^2 \quad (8)$$

$$\frac{t}{q_t} = \frac{1}{k_2 q_e^2} + \frac{t}{q_e} \quad (9)$$

$$q = k_d t^{1/2} (+C) \quad (10)$$

Thermodynamic investigations elaborated in S12 were assessed using Equation. (11 – 13), where $Ke(L/g)$ is the adsorption equilibrium, ΔH°(J /mol) and ΔS° (J.K/mol) are the standard enthalpy and entropy, and ΔG° (J/mol) the standard Gibbs free energy, correspondingly.

$$Ke = qe/Ce \quad (11)$$

$$lnKd = (\Delta H^\circ) / RT \quad (12)$$

$$\Delta G^\circ = \Delta H^\circ - \Delta S^\circ T \quad (13)$$

The gliadin extraction and adsorption experimental protocols used in this study are summarised in Fig. 1.

3. Results and discussion

3.1. Scanning electron microscopy and energy dispersive X-ray spectroscopy

Fig. 2 shows the SEM analysis of gliadin blended composites. The SEM micrograph in Fig. 2 (a) indicates that gliadin has non-porous fibrillar morphology externally. However, a magnified cross-section of the protein (Fig. 2 (b)) shows irregular honeycomb internal porous structure with void spaces. Fig. 2 (c & d) shows a fragment of gliadin thoroughly mixed with TiO_2 particles implying successful incorporation of TiO_2 into gliadin. In addition, gliadin blended with α–Fe_2O_3 and AgFe–TiO_2 show different textural morphologies with fillers well dispersed in gliadin suggesting that α–Fe_2O_3 and AgFe–TiO_2 were fused into void spaces of the protein framework leading to the formation Fe_2O_3@gliadin and AgFe–TiO_2@gliadin composites with individual powder shapes/morphologies exhibited in Fig. 2(e and f).

The EDS micrographs in Fig. SF1 (a-f) show all elements including Ag, Fe, Ti, C, N, and O were present in AgFe–TiO_2 @ Gliadin composite implying that the metal oxides TiO_2, α-Fe_2O_3 and AgFe–TiO_2 were successfully embedded in gliadin. The elemental trends on weight and atomic percentages during the protein modification were surveyed by EDS analysis coupled to SEM and the results are presented in Table ST1. From the pristine gliadin, the weight percentage of O, C, and N recorded were 23.83, 56.67 and 19.5 %, respectively. Traces of Ti in TiO_2@-Gliadin reached 48.2%. However, the O percentage (23.83 %) in gliadin increased to 37.04 % in TiO_2@Gliadin while that of C (56.67) and N (19.5) in gliadin decreased to 10.63 and 4.14% in TiO_2@Gliadin, respectively. This implies that the incorporation of TiO_2 (O–Ti–O) into gliadin by mechanical stirring was well achieved and the lower C and N indicate the dilution of the protein by the addition of the metal and oxides as fillers. The weight percentage ratio of O and N in unmodified gliadin is approximately 1:1 but changed to 9:1 in the TiO_2@Gliadin composite. On the other hand, the weight ratio of O and C (1:2) in gliadin altered to 3:1. This signifies that more of the Ti and O imported from TiO_2 diluted C and N resulting in a composite. Similar trends were observed in the case of $AgFeO_3$ @Gliadin except that the ratios of O and C, O and N appeared to be 5:1 and 6:1, respectively suggesting that abundant O in $AgFeO_3$ @Gliadin originated from both Ag_2O and Fe_2O_3 as AgF_2O_3 at the expense of C and N. These mitigations were further detected for AgFe–TiO_2@ Gliadin whereby the O and C, O and N ratios changed to 2:1 and 5:1, correspondingly. These outcomes infer that the blending of gliadin with metal oxides via constant mechanical stirring was well achieved and follows the changes in morphologies observed in SEM analysis in Fig. SF1.

3.2. X-ray diffraction

Fig. 3d displays the XRD diffraction patterns of gliadin blended composites. The unmodified gliadin existed solely in the amorphous phase and broad peaks were visible at $2\theta = 8^\circ$ and 19°, like the report of Gulfam et al. (2012). The diffraction spectrum of TiO_2@gliadin exhibited both strong reflections of amorphous gliadin at $2\theta = 8^\circ$ and anatase

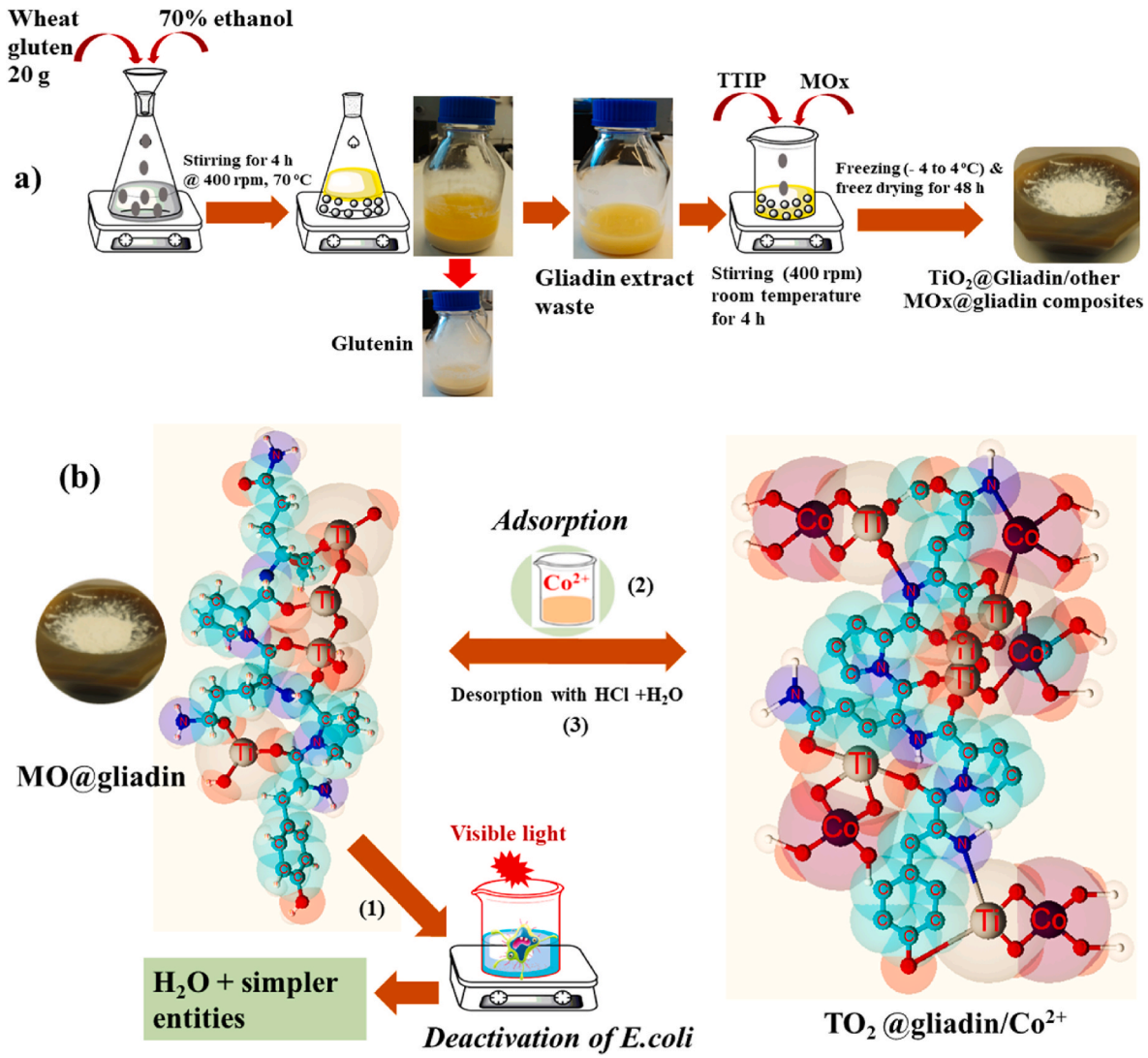

Fig. 1. Experimental protocols for (a) extraction of gliadin waste and blending with metal oxides, (b) inactivation of *E. coli* and removal of Co^{2+} from water.

((JCPDS, No. 00-021-1272) phase of TiO_2 characterised by diffraction peaks 2θ = 48.24° (200) and 62° (213) which relate to the body-centered tetragonal lattice arrangement of the mineral anatase phase (Mouele et al., 2020). In both $AgFe_2O_3$@gliadin and AgFe–TiO_2@gliadin composites, iron oxide patterned at 2θ = 29.3° (012), 32.16° (104) and 33.92° (110) corresponded to hematite phase (α-Fe_2O_3). While the coexistence of silver was depicted at 2θ = 38° (111), 44.5° (200), and 64.5° (200) consistent with previous research (Balasubramanian et al., 2014; Xu et al., 2015). The anatase TiO_2 was also traceable in AgFe–TiO_2@gliadin at 2θ = 48.24° (200); the observable amorphous phase of gliadin was still present in $AgFe_2O_3$@gliadin and AgFe–TiO_2@gliadin at 2θ = 8° signifying that metal oxides TiO_2 and α– Fe_2O_3 were successfully blended in gliadin and their insertion did not impact on the physical structure of the protein, which remained intact.

3.3. Fourier Transform Infrared

The absorption bands of all composites depicted by attenuated total reflectance-Fourier Transform Infrared (ATR-FTIR) were summarised in Table ST2 and plotted in Fig. 3b. The absorption frequencies of bare gliadin were mainly identified in three regions 2700–3700, 1200–1800, and 500–1200 (cm^{-1}), respectively. The stretching vibrations peak of O–H accounting for intermolecular attached hydroxyl group and N–H stretching vibrations characteristics of amides A of polypeptides and amino acids were located at 3700–2700 cm^{-1} for all samples except that their intensities decreased in the blended gliadin composites suggesting the possible formation of hydrogen bonding between gliadin functional groups and that of the blending agents (Popov et al., 2017). In the region 1200–1800 cm^{-1}, the following C–N; C–O; C]O and N–H stretching vibration groups characteristic of carboxylic, amino acid, and amides (primary and secondary) in unmodified gliadin were identified (Pereira et al., 2010; Hoque et al., 2011; Yang et al., 2021). Furthermore, the unsaturation and saturation stretching vibrations mainly C]C and C – C are depicted in the fingerprint range 500–1200 cm^{-1}. For TiO_2@gliadin composite, traces of C–N, –C–C, C–O, and C]O stretching were evidenced at 1200–1800 cm^{-1} at low intensities except for C]O that remained persistent indicating that interactions between gliadin and TiO_2 were independent of C]O stretching. The sharp bands subsequently formed in the lower range 300–1200 cm^{-1} were ascribed to Ti – O –Ti and O–Ti–O groups. This implied that the incorporation of TiO_2 into gliadin was certainly induced by electrostatic or hydrophobic interactions (Antoniou et al., 2015), suggesting that TiO_2 probably coordinated to other oxygen or nitrogen atoms leading to the diminishment of = C–N and C]O peak intensities and hence the formation of Ti – O –Ti and O–Ti–O stretching around 300–1200 cm^{-1}. This later scenario was remarkable in $AgFe_2O_3$@gliadin composite where the insertion of α–Fe_2O_3 into gliadin structure displaced C–N and C]O stretching in the 1200–1800 cm^{-1} range, resulting in the formation of Ag–O, Fe–O,

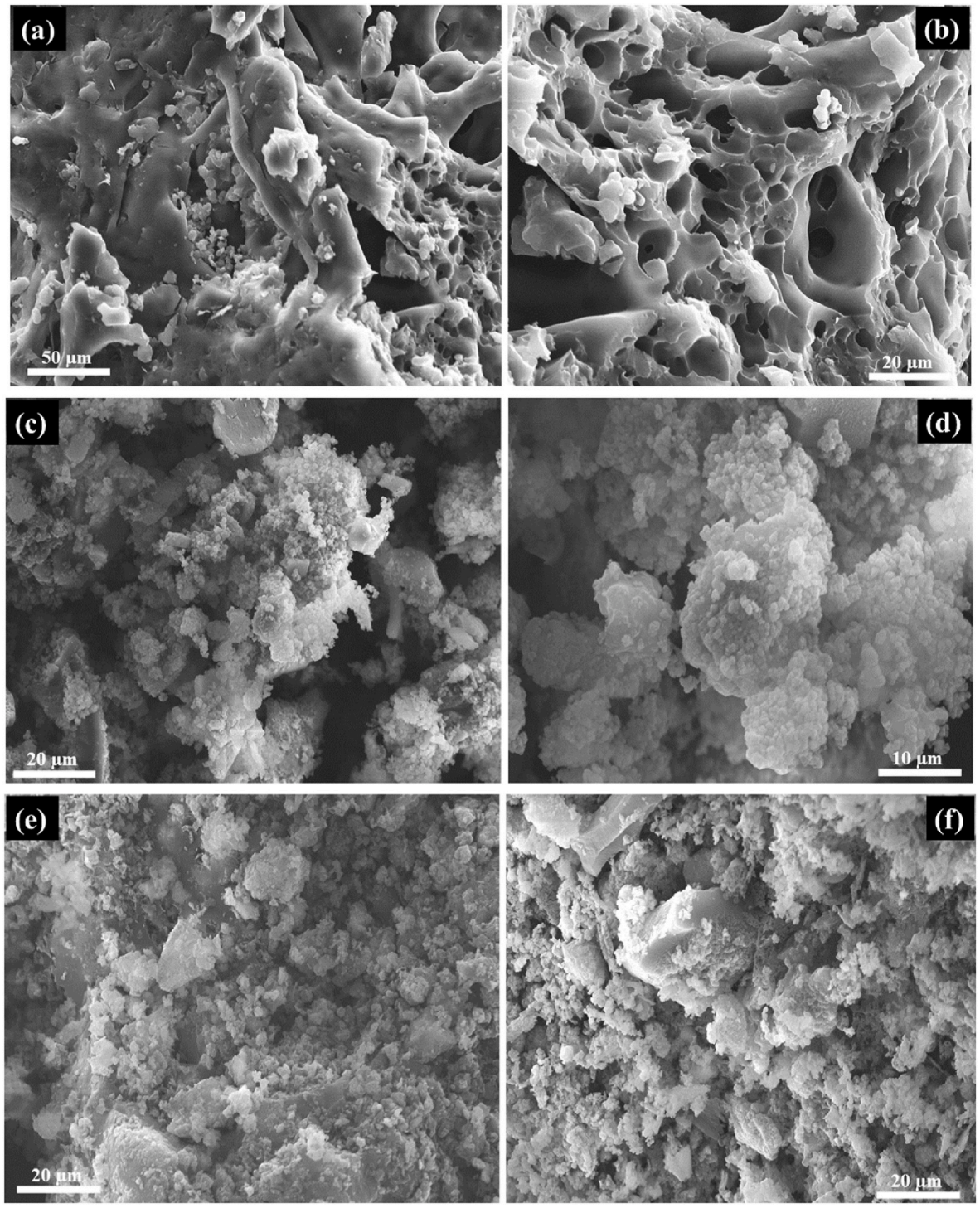

Fig. 2. SEM micrographs of (a & b) Gliadin, (c & d) TiO_2@gliadin, (e) Ag_2FeO_3@gliadin, and (f) AgFe–TiO_2@gliadin composites.

Ag–Fe–O, Ag–O–Fe and Ag–Fe functional groups characterised by strong absorption bands between 300 and 1200 cm $^{-1}$. Similarly, during the incorporation of co-doped AgFe–TiO_2 into wheat gliadin, the decrease of = C–N; O–H; C–O; C]O and N–H band intensities in 1200–1800 cm $^{-1}$ resulted in the successive appearance of strong Ag–Fe–O, Ag–O–Fe, Ag–Fe, O–Fe–O, and O–Ag–O stretches between 700 and 1200 cm $^{-1}$ and moderate Ag–O, Fe–O, Ti –O–Ti and O–Ti–O vibrations in 300–680 cm $^{-1}$ assortment. These phenomena indicate that the insertion of metal oxides TiO_2 and α-Fe_2O_3 into gliadin framework resulted in protein dispersion initiated by hydrophobic effects during conversion of formal functional groups and the formation of hydrogen bonds (Liu et al., 2018; Chen et al., 2021). This consequently implies that blending of gliadin successfully led to the development of novel composites aimed at effective removal of $Co^{2+}$and detoxification of bacterial wastewater.

3.4. Thermal gravimetric analysis

Blended gliadin composites were analysed by TGA and its derivative to examine the weight loss and thermal degradation steps of the composites. The outcomes in Fig. 3c show that thermal weight loss of unmodified gliadin reached 80 % between 160 and 800 °C, with the main decomposition peak centered at 330 °C and a residual mass of less than

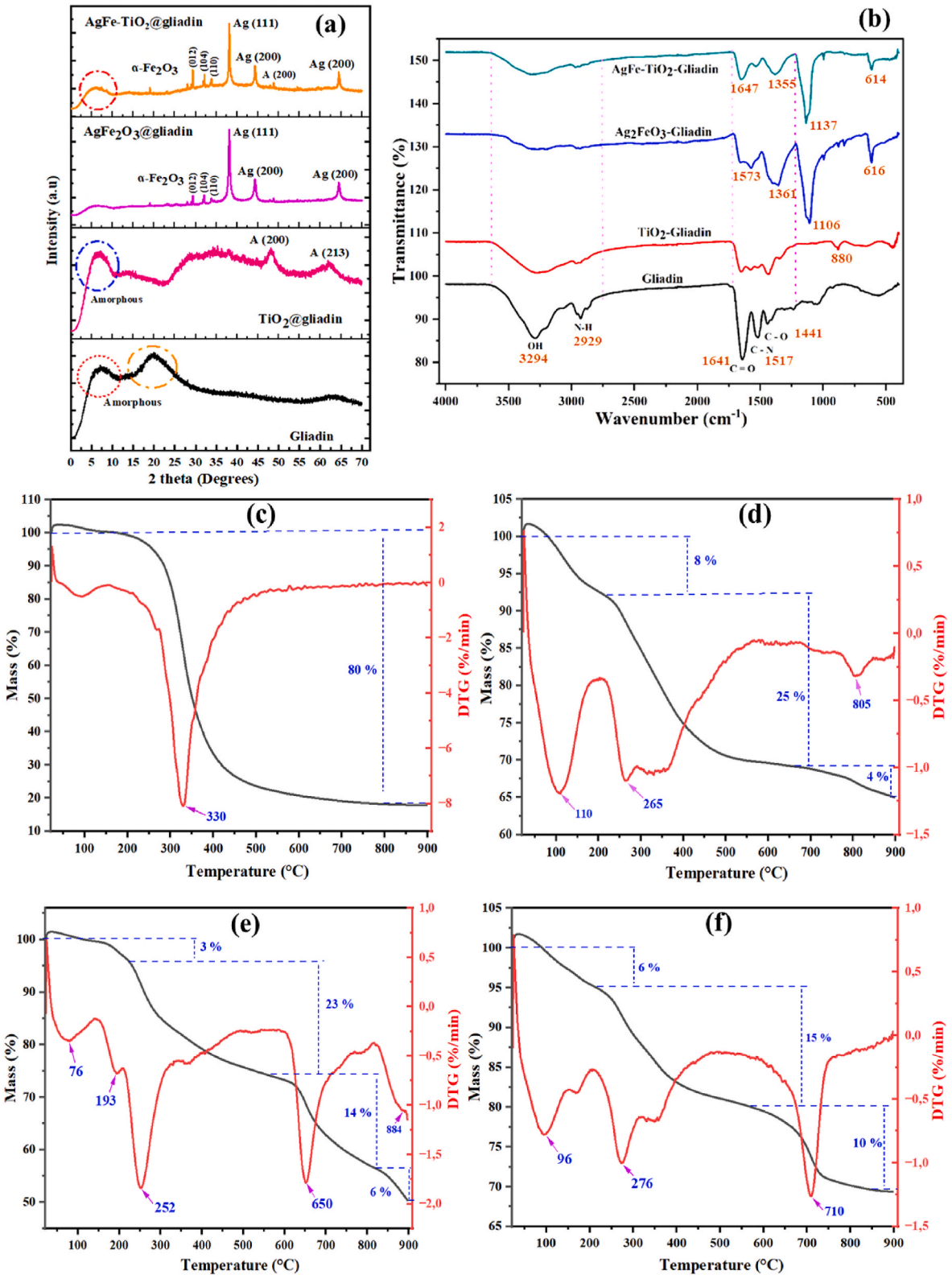

Fig. 3. (a) X-ray diffraction (XRD), (b) Fourier transform infrared spectroscopy (FTIR), (c–f) thermal gravimetric (TGA) and differential thermogravimetry (DTG) plots of gliadin blended composites (c) Gliadin, d) TiO_2@gliadin, e) $AgFe_2O_3$@gliadin, and f) AgFe–TiO_2@gliadin.

10% remaining at 800 °C. The thermal degradation of TiO_2@gliadin, $AgFe_2O_3$@gliadin, and AgFe–TiO_2@gliadin followed multistep processes. A weight loss of 8% was observed between 78 and 200 °C for TiO_2@gliadin, and 25 % weight loss occurred between 222 and 665 °C, with a further loss of 4.65% between 760 and 890 °C. A residual mass of about 65% remained at the terminal temperature of 890 °C. When, the inclusion of TiO_2 improved thermal stability by a factor of 2.5 as compared to bare gliadin. This could be ascribed to hydrophobic and possibly covalent interactions between TiO_2 and gliadin functional groups (Zhang et al., 2003a). In Fig. 3e, the thermal degradation of

$AgFe_2O_3$@gliadin gradually increased from 3 to 24 % between 60 and 160 °C and 165–567 °C, respectively, and weight loss of 14% between 590 and 820 °C, and 6 % between 815 and 890 °C, were observed, with a residual mass of around 50% remaining at the terminal temperature. In comparison with unmodified gliadin, the addition of $AgFe_2O_3$ in gliadin enhanced the thermal stability by a factor of 1.7 (80% vs 47%) due to potential ionic and hydrophobic interactions between $AgFe_2O_3$ and gliadin. A similar thermal trend was observed in the case of AgFe–TiO_2@gliadin composite (Fig. 3f) with a weight loss of 6 % between 40 and 205 °C and 15 % between 215 and 500 °C, respectively, which decreased to 10 % between 655 and 890 °C, with a residual mass of about 70% remaining at the terminal temperature. These results show that blending gliadin with AgFe–TiO_2 decreased the thermal stability by a factor of 2.6 (80% vs 31 %). During the composting of the materials, gliadin nonpolar groups may become favourable to the complexation with TiO_2 and Fe_2O_3 possibly through hydrogen bonding, hydrophobic interactions, covalent, and ionic bonding (Madhan et al., 2005; Tsai and She, 2006). But these did not apparently enhance the thermal stability of gliadin (Zhang et al., 2003b). Moreover, the steric and surface charge repulsion between metal oxides and protein probably weakened the resistance of the novel composites against disintegration, which oppose previous claim reported in (Xue et al., 2018).

3.5. Surface area determination

The surface area and BET isotherms of gliadin blended composites that are shown in Fig. 4(a–c) define their pore size, pore volume and specific surface area that are displayed in Table ST3. The results indicate that blended composites with lower surface areas exhibited lower pore volumes. The specific surface area of TiO_2@gliadin, $AgFe_2O_3$@gliadin, and AgFe–TiO_2@gliadin ranged from 11. 80, 1.45–150.45 m^2g with corresponding pore volumes of 0.062, 0.007, and 0.092 cm^3/g, respectively. The surface area of unmodified gliadin was 0.170 m^2/g with a very poor pore volume of 0.0002 cm^3/g defined by particle aggregation as claimed in previous investigations (Liao et al., 2016b). These outcomes show that the surface area of TiO_2@gliadin, $AgFe_2O_3$@gliadin and AgFe–TiO_2@gliadin are 11, 2, and 100 times higher than that of the bare gliadin owing to the dispersion of gliadin. The isotherms of TiO_2@gliadin and $AgFe_2O_3$@gliadin in Fig. 4 (a & b) correspond to type II isotherms, which are characteristics of finely divided nonporous blended composites with a sharp increase in adsorption and desorption at low relative pressure followed by steady phase and no delay or discontinuation in the adsorption/desorption cycle. Nevertheless, the outcomes in Table ST3 indicate that TiO_2@gliadin with a pore size of 21.7815 nm is expected to be mesoporous, like $AgFe_2O_3$@gliadin with a pore diameter of 19.0797 nm. On the other hand, the plot of AgFe–TiO_2@gliadin in Fig. 4c displays a type IV isotherm assigned to mesoporous blended material. However, its feature hysteresis loop could be generated by the capillary condensation of the adsorbate in the mesopores of the composite.

3.6. Zeta potential

The surface charges of gliadin composites were investigated by the zeta potential of composites dissolved in deionised water and the results are shown in Fig. 4d. The outcomes indicate that the surface charge of gliadin and AgFe – TiO_2@gliadin changed from positive to negative with the increase in pH. The isoelectric point (IEP1) of gliadin could be

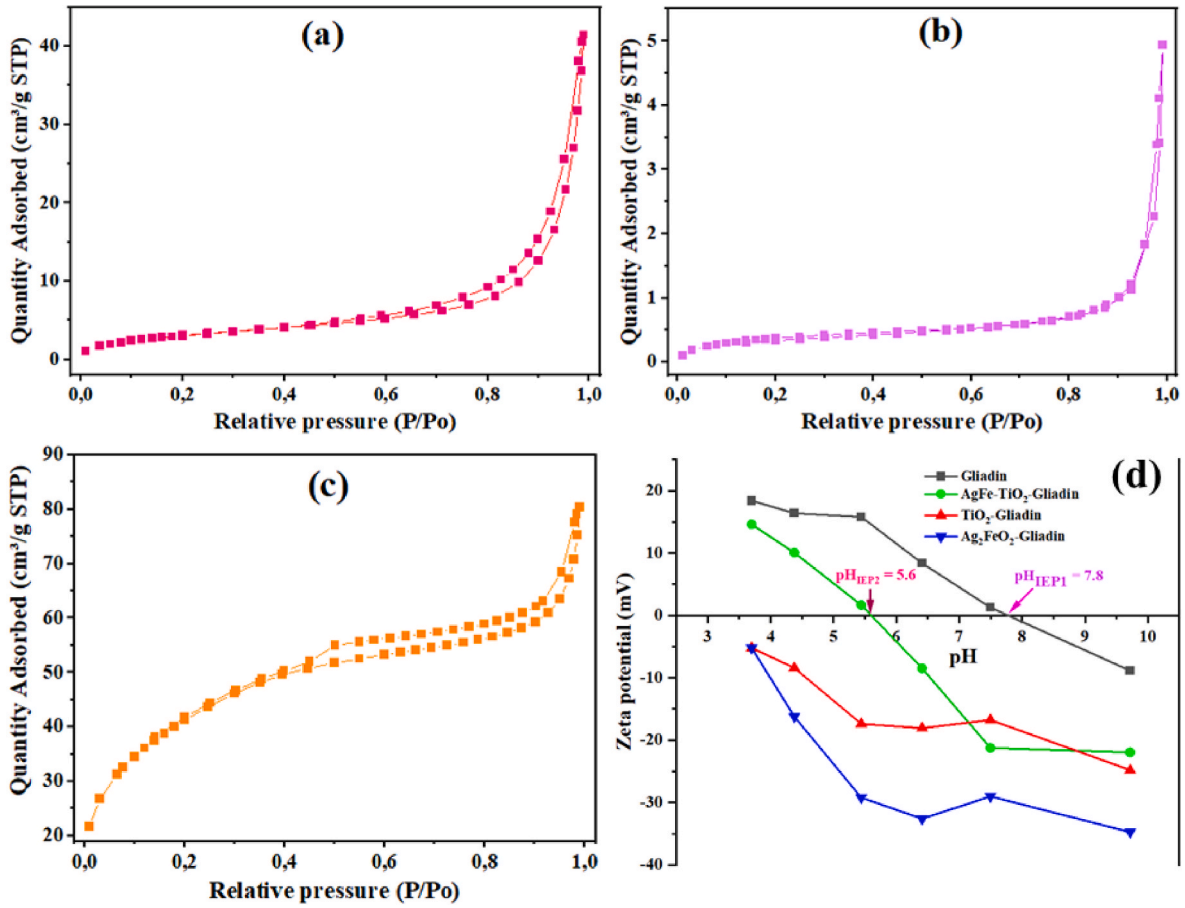

Fig. 4. Nitrogen adsorption and desorption isotherms of (a) TiO_2@gliadin, (b) $AgFe_2O_3$@gliadin, and (c) AgFe–TiO_2@gliadin, and (d) zeta potential of gliadin blended composites.

observed around 7.8 which is one magnitude higher than the 6.5 reported in previous studies (Joye et al., 2015a; Joye et al., 2015b; Wu et al., 2018b) and implies that at pH < 7.8, gliadin is positively charged and may oppose cations being targeted; while at pH > 7.8 the surface of gliadin is negatively charged and is expected to improve the affinity towards selected cations.

The IEP2 of AgFe–TiO_2@ gliadin was located at a pH of 5.6 and hence lower than that of gliadin. On the other hand, the zeta potential of both TiO_2@gliadin and $AgFe_2O_3$@gliadin was negative in the pH range of 3.5–9.5 and slightly increased in absolute magnitude with an increase in pH. This signified that the surfaces of the later composites were populated by negative charges and favourable for the adsorption of positively charged species. Gliadin showed a negative trend between pH 3.5 and 9.5. The incorporation of TiO_2 and $AgFe_2O_3$ into gliadin resulted in blended composites with noticeable stability between pH 5.5 and 7.5 that gradually was lost as the solution pH increased. AgFe–TiO_2@gliadin exhibited both positive and negative ζ-potential values. This was extensively supported by the back shifting of AgFe–TiO_2@gliadin IEP2 to 5.6 being lower than that of unmodified gliadin.

As much as the deamination of gliadin occurs via conversion of amine groups (Moraveji), the blending functionalisation of gliadin was ascribed to hydrogen bonding, covalent bonding, or weak surface and electrostatic forces of amino and related groups with metal oxides (MOs) forming novel complexes. Hydrophobic aggregation of neat gliadin resulted in poor surface area and inadequate pore volume. Its functionalisation resulted in dispersed materials with improved surface area and pore volumes and interesting changes in surface charge.

The AgFe–TiO_2@gliadin blended composites appeared stable at the pH range of 7.5–9.5 while unmodified gliadin was extremely unstable at pH 7.5. This was mainly due to the aggregation of gliadin extract at pH 7.5–8 and blended AgFe–TiO_2@gliadin at pH 5.5–6. In the pH range of 7.5–9.5, the ζ-potential values of blended gliadin composites were recorded between −18 and −38 mV indicating a high degree of dispersion. This is in line with Maryam Moraveji et al. (Moraveji) who testified that high absolute values of ζ-potential imply abundant repulsions between colloidal species that prevent aggregation and hence sustain the stability of particles.

However, Freitas & Müller, (Freitas and Mü, 1998) claimed that 30 mV is likely the threshold absolute value of the ζ-potential that dictates the stability of charged colloidal structures. For ζ-potential absolute values above 30 mV, dispersions could be disrupted and result in particles agglomeration and precipitation in lower ionic conditions. In the current study, this scenario was observed with $AgFe_2O_3$@gliadin blended composite where the absolute ζ-potential evidenced around 38 mV led to a light blue precipitate of aggregated particles in alkaline media.

3.7. Antimicrobial bioassay

The first aspect of gliadin blended composites multifunctionality was evaluated by assessing the antibacterial properties vital for water purification. This was achieved up on inactivation of bacterial culture of *Escherichia coli* under dark and visible light conditions (Fig. 5). The statistical analysis (ANOVA) of the antibacterial tests with gliadin composites is shown in Table ST4.

In the dark conditions, TiO_2@gliadin exhibited a significant reduction in *E. coli* density after 24 h of incubation in comparison to all other composites and control ($P < 0.05$) (Fig. 5a, Table ST4). The observed activity of TiO_2@gliadin in the dark could be due to different reasons. First, *E. coli* cells are negatively charged due to the presence of lipopolysaccharides layer (REF). Interactions between the cell wall of the bacteria and TiO_2@gliadin could promote cell death. Therefore, the antimicrobial activity could be due to the presence of metal ions (Moraveji; Freitas and Mü, 1998). On the other hand, the aqueous mobile metal ions such as Ag^+ and Fe^{2+} potentially incapacitate various enzymes and/or directly damage DNA leading to cell destruction (Prabhu and Poulose, 2012). Alavi & Yarani (2022) reviewed various approaches on the development of antibacterial metal oxides (MO) or metal nanoparticles (MNPs). In their report, the authors informed that the two principal mechanisms involved in the killing of bacteria include direct binding of MO/MNPs to biological macromolecules which results in cell wall damage, causing destruction of the bacterial membrane followed by electron transport that disrupts nucleic acids, proteins, or enzymes. The second mechanism is the indirect generation of reactive oxygen species (ROS) mainly $O_2^{\cdot-}$, $^1O_2^-$, H_2O_2 and $OH^{\cdot}$ inside the bacteria cell membrane leading to DNA damage and total inhibition (Alavi and Yarani, 2022). These scenarios were possibly responsible for the slight antibacterial activity of gliadin functionalised composites under dark conditions plotted in Fig. 5a.

After 24 h of incubation under light conditions (Fig. 5b), all composites showed a significant reduction in *E. coli* density in comparison with unmodified gliadin and control ($P < 0.05$). The lowest density of bacteria was observed in the case of TiO_2@gliadin. The ANOVA analysis (Table ST4) revealed that TiO_2@gliadin substantially reduced the density of *E. coli* to 50.5% in comparison to the control *(Tukey, Post-hoc $p < 0.05$)*. This can be explained by the photocatalytic activity of AgFe–TiO_2 catalyst dopant functionalised into gliadin and the subsequent production of reactive oxygen species (ROS) in aqueous gliadin composites - *E*

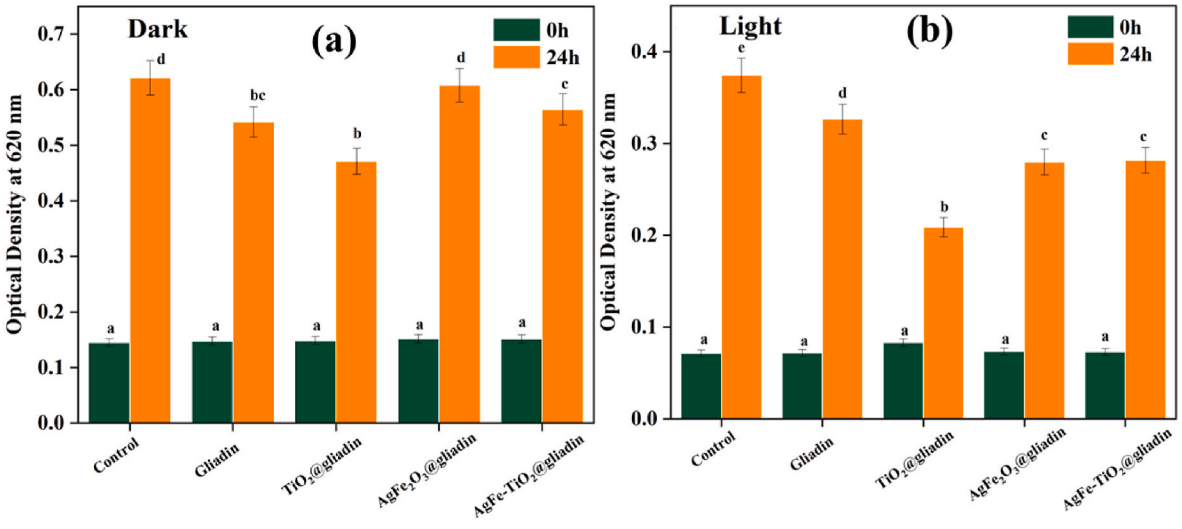

Fig. 5. *E. coli* evolution on gliadin blended composites in (a) dark and (b) light after 0 and 24 h. Data were means ± SD; n = 3.

coli matrix (K.Y et al., 1998). Certainly, when gliadin composites matrix is exposed to visible light, the abovementioned ROS are generated via activation or electron promotion from TiO_2 and dopants valence bands to the conduction bands. In this regard, Ag_2O and Fe_2O_3 used as dopants retarded electron-hole pairs recombination and favored the storage of charge carriers (e^-) that were disseminated around the surface of TiO_2@gliadin composite. On the one hand the produced electrons diffuse into the aqueous gliadin composites - *E coli* matrix and reduce O_2 producing various ROS such as $O_2^{\cdot-}$,$^1O_2^-$, H_2O_2 and $OH^{\cdot}$. While the active holes (h^+) pairs on TiO_2 and dopants valence bands oxidize H_2O molecules to $OH^{\cdot}$. Altogether, the produced ROS attacked the cell membrane of the *E. coli* followed by DNA disruption and death (Alavi and Yarani, 2022).

$AgFe_2O_3$@gliadin and AgFe–TiO_2@gliadin showed adequate bacterial reductions in the density of *E. coli* of 25.2 and 24.7% as compared to 12.8% with gliadin only, respectively with respect to the control after 24 h ($P < 0.05$). However, there were no significant differences between these treatments (Table ST4) (ANOVA, $p > 0.05$). Gliadin on the other hand had the lowest bacterial inhibition (Fig. 5 (a &b). The poor attractive charges on its surface could be ascribed to the excess of nutritious carbon content in gliadin (Wanag et al., 2018a). Indeed, the EDS results shown in Table ST1, indicate that the carbon content was 10.36 % for TiO_2@gliadin, 11.77% and 20.41% for $AgFeO_3$ @gliadin and AgFe–TiO_2@gliadin, and 56.67% for gliadin itself, correspondingly. According to Agnieszka Wanag et al. (2018b) elevated carbon content in catalyst materials obstructs the interaction between C and Ti and hinders the activity of the semiconductor s' surface which further inhibits photocatalytic efficacy. As a result of these mitigations, the release of free radicals in the solution could have been impeded, resulting in a decrease in antibacterial effectiveness.

When compared to normal MO, Alavi and Yarani (2022) claimed that an excessive dose of antibacterial NPs could result in minimal biocompatibility and cytotoxicity in biological environments. Therefore, coupling photocatalytic NPs with other biocompatible antibacterial constituents is a promising method to engineer novel materials with advanced physicochemical properties. So, the co-doping of Ag_2O and Fe_2O_3 in TiO_2 and their subsequent dispersion into gliadin covered in this study is an adequate procedure for development of multifunctional antibacterial protein-MO composites.

3.8. Adsorption studies

3.8.1. Effect of initial solution pH and concentration

To establish their multifunctional characteristics, the adsorption properties of gliadin blended composites were evaluated, in addition to the antibacterial activity examined in the previous section. The effect of initial pH and concentration on the removal efficiency (%) and adsorption capacity (q_e, mg/g) of Co^{2+} by gliadin and gliadin blended composites described in supplementary data Text S4 (Equations (1) and (2)) was assessed by altering the solution pH from 3 to 8, and the initial concentration from 25 to 400 mg/L, and the results are displayed in Fig. 6. Fig. 6 (a) demonstrates that regardless of the pH region, 99.99%

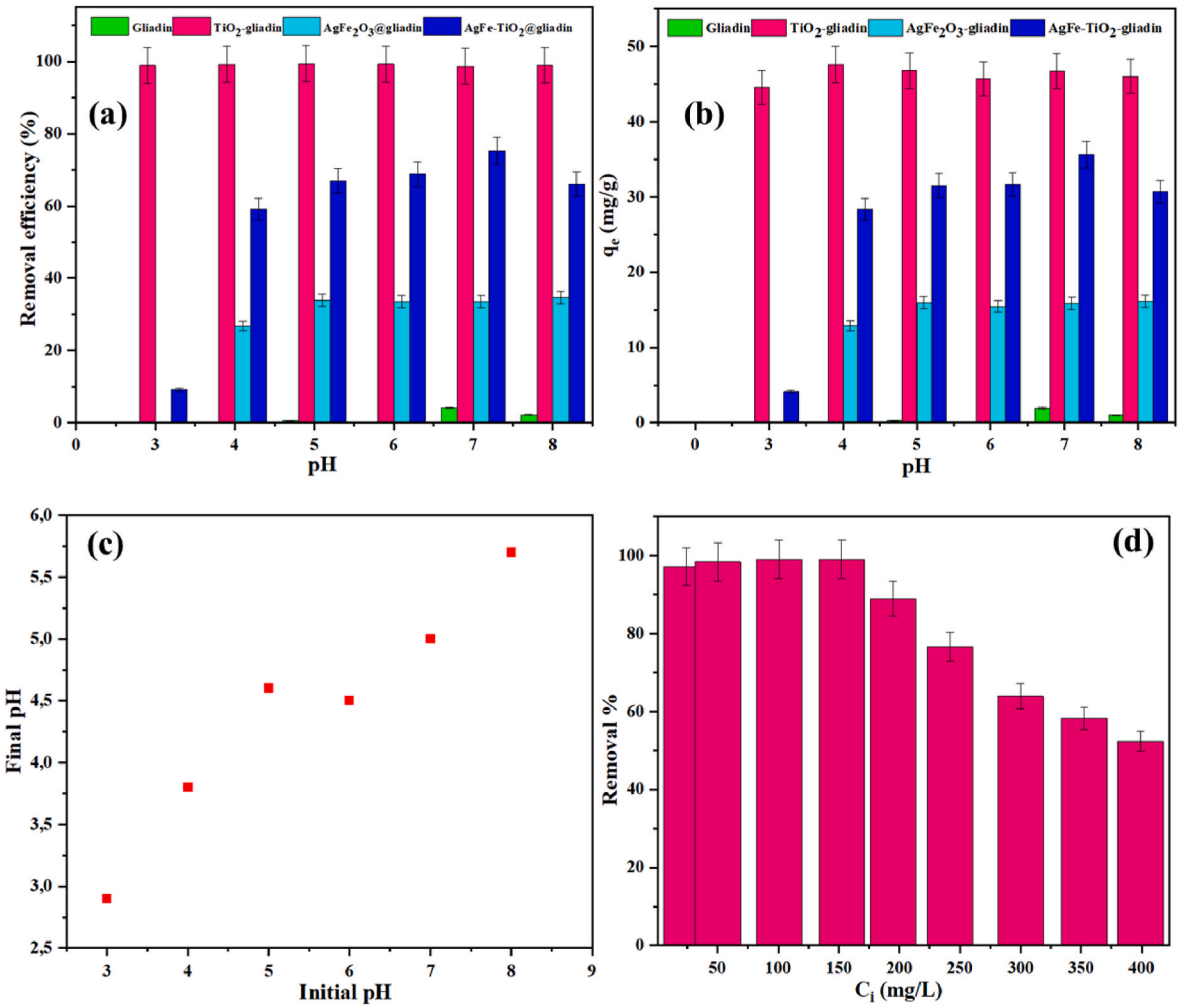

Fig. 6. (a & b) effect of pH on removal efficiency and adsorption of Co^{2+} by gliadin blended composites (n = 2), (c) behaviour of initial solution pH before and after adsorption, and (d) effect of Co^{2+} initial concentration (m = 10 mg, V = 10 mL, t = 1440 min, n = 2).

of Co^{2+} removal was achieved with TiO_2@gliadin composite indicating that solution pH in the range of 3–8 did not impact on the retention efficacy of Co^{2+} (Pongkitdachoti and Unob, 2018a). On the hand, 70% removal was attained with AgFe -TiO_2@gliadin at pH 7, while 26% with $AgFe_2O_3$@gliadin at pH 5–8, and about 5% retention with gliadin at pH 7, respectively. These removal efficiencies indicated that the solution pH affected both the surface charge and textural chemistry of the blended composites (Mengesha et al., 2022a). According to zeta potential diagnostics in Fig. 5d for pH range below the isoelectric points IEP1 = 7.8 and EPE2 = 5.6, gliadin and AgFe–TiO_2@gliadin are positively charged and consequently show poor interactions towards Co^{2+} which further indicate minimal electrostatic interactions. Despite having a negative charge in the pH range tested, the $AgFe_2O_3$@gliadin composite showed only moderate removal efficiency. A similar trend was observed in the case of uptake capacity q_e (mg/g) in Fig. 6 b whereby the highest Co^{2+} adsorption capacity of 48 mg/g was reached with TiO_2@gliadin at pH 4 versus 36 mg/g for AgFe–TiO_2 at pH 7, 15 mg/g for $AgFe_2O_3$@gliadin at pH 5–8 and roughly 2 mg/g for gliadin at pH 7, correspondingly. Fig. 6 c indicates that solution pH declined from the initial domain of 3–8 to lower values by a magnitude of 2 (for initial pH region of 6–8) and down to the lowest values by magnitude of 0.5 (for initial pH region of 3–5) after adsorption. These observations were probably due to the presence of protons released during the complexation of Co^{2+} and TiO_2@gliadin functional groups (OH, CO, O–Ti–O, etc.) (Pongkitdachoti and Unob, 2018b). Instead, Fig. 6d shows that complete removal of Co^{2+} was achieved at concentrations range of 50–200 mg/L, nevertheless 100 mg/L was selected as the optimum concentration to ease the ICP analysis. These outcomes indicate that the surface properties of adsorbents and solution chemistry significantly impact on the removal of metal ion in the solution (Mengesha et al., 2022b). Consequently, TiO_2@gliadin was selected as the suitable composite for extended experiments for the adsorption of 100 mg/L Co^{2+} in an acidic environment (pH 4).

3.8.2. Adsorption isotherms

The adsorption isotherms including Langmuir, Freundlich and Temkin models described in supplementary materials Text S5 - Text S7 (Equations (3)–(5)) were used to assess the affinity, surface heterogeneity sites and multilayer adsorption, and the interaction between TiO_2@gliadin composite and Co^{2+}, respectively. Fig. 7a indicates that the removal of Co^{2+} in the solution was thoroughly illustrated by the Langmuir isotherm model (R^2 = 0.958) with a maximum adsorption capacity (q_m) of 96.996 mg/g (Table ST5) which closely corroborates the experimental uptake capacity (q_e, exp = 101 mg/g). In contrast, Freundlich (R^2 = 0.825) and Temkin (R^2 = 0.858) (Table ST5) did not fit the experimental results nicely. Their L-type isotherms without strict plateau propose a progressive saturation of TiO_2@gliadin composite (Covelo et al., 2007a). The Langmuir H-type isotherm indicates strong interactions between Co^{2+} and TiO_2@gliadin (Covelo et al., 2007b). Therefore, these outcomes assume that the retention of Co^{2+} followed monolayer coverage and constant binding energy between TiO_2@gliadin surface and Co^{2+} cation. The K_L constant of 0.726 L mg^{-1} in Table ST5 possibly suggests strong affinity between the absorbent and absorbate associated with elevated energy for the uptake of Co^{2+}. The

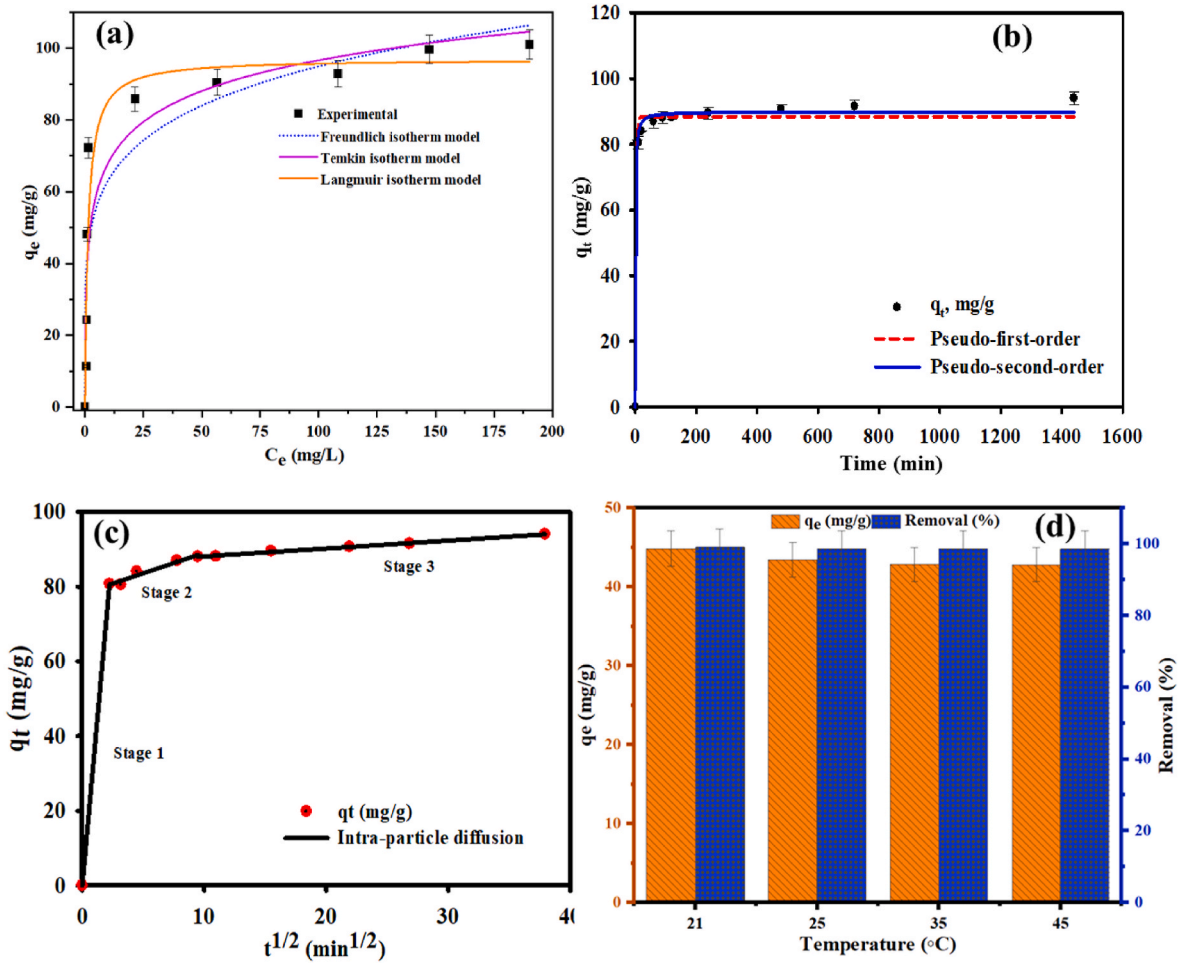

Fig. 7. (a) Adsorption isotherms, (b) Kinetics, and (c) Intra-particle diffusion model parameters acquired during adsorption of Co^{2+} by TiO_2@gliadin blended composite (C_o = 100 mg/L, V = 10 mL, pH = 4, m = 10 mg).

interface of Co^{2+} on TiO_2@gliadin possibly occurred via hydrogen bonding, hydrophobic interactions, or covalent bonding with OH, C]O, T–O, etc. groups of the blended composite.

3.8.3. Kinetics investigation

The kinetic of adsorption of Co^{2+} by TiO_2@gliadin blended composite was examined using pseudo-first-order, pseudo-second order, and intraparticle diffusion models whose experimental details are shown in supplementary data Text S8 - Text S11 (Equation (6) -10), correspondingly.

Fig. 7a shows that in the primary stage of adsorption, about 91.75% of Co^{2+} was removed after 90 min and slightly increased to 92.19% followed by saturation within 120 min of sorption. This is ascribed to the coactive effect of surface chemistry and pore texture of TiO_2@gliadin composite (Mengesha et al., 2022b). The following pseudo-first order (PFO), pseudo-second order (PSO), and intra-particle diffusion models (Fig. 7b and c) were used to fit the experimental kinetic data (De Andrade et al., 2018; Marçal et al., 2015; Santoso et al., 2020; Zhang et al., 2021) and the derived kinetic parameters are recorded in Table ST6. In Fig. 7b, the adsorption of Co^{2+}in solution occurred gradually and reached equilibrium after 120 min. This progressive retention of Co^{2+} was probably due to the multistep adsorption scenarios or the slow dissemination of adsorbate into the non-uniform mesopores of the TiO_2@gliadin composite. The adsorption of Co^{2+} conformed to a pseudo-second-order kinetic model defined by a correlation coefficient (R^2) of 0.993. The adsorption capacity of Co^{2+} (q_{e2} = 89.86 mg/g) dictated by the pseudo-second-order scheme at equilibrium was near to the experimental data (q_e, exp = 101 mg/g). The intra-particle diffusion model (Fig. 7c) shows that the removal of Co^{2+} certainly happened in three major diffusion steps. The first stage ($R^2 = 1.000$) characterised by a very fast adsorption phase marked by a very sharp initial slope is related to diffusion when adsorbates are transferring from the bulk to surface (Beltrame et al., 2018). This is followed by a quick and short pore diffusion phase (stage 2, $R^2 = 0.948$), and a prolonged equilibrium phase (stage 3, $R^2 = 0.995$).

Table ST7 shows that the first phase occurred substantially more rapidly than the second and last steps as indicated by the diffusion rate $K_{i1} = 36.084 > K_{i2} = 1.089 > K_{i3} = 0.211$ mg/gmin$^{0.5}$, so the adsorption rate is mostly controlled by the first step (Viegas et al., 2014; Qiu et al., 2009).

3.8.4. Thermodynamics

The impact of temperature varied from 21 to 45 ˚C on sorption of Co^{2+} by TiO_2@gliadin composite was evaluated at the applied conditions. The thermodynamic study for the removal of Co^{2+} is theorized in supplementary materials Text S12 while the linear trend *Ke* vs. 1/T described in Equations 11–13 was used to determine ΔH°, ΔS° and ΔG°, respectively (Liu et al.). Fig. 7d shows that the removal efficacy (%) of Co^{2+} slightly decreased with an increase of temperature. That is a retention 99.1% achieved at 21˚C decreased slightly to 98.75, 98.74 and 98.6 % when the temperature was raised to 25, 35 and 45 ˚C, respectively. This could be attributed to possible protonation and inhibition of the active sites of TiO_2@gliadin composite that are supposed to induce strong interactions with Co^{2+} in acidic conditions. This also affected the adsorption capacity q_e in Fig. 7d that slightly dropped from 45 to 43.8 mg/g as temperature changed from 21 to 45 ˚C, accordingly. The values of estimated thermodynamic parameters are presented in Table ST8. The negative $\Delta G^\circ = -9.677$ *kJ*/mol observed implies spontaneous and favourable adsorption. While $\Delta H^\circ = -123$ kJ/mol and $\Delta S^\circ = 0.490$ J.*k*/*mol* indicate that adsorption of Co^{2+} was an endothermic process, and both a decrease and increase in solid/solution interface randomness were experienced, respectively (Kasperiski et al., 2018). The ΔH° value being less 40 kJ/mol suggests physisorption process. The slight decrease of ΔG° observed implies the increase of temperature unfavoured Co^{2+} removal process.

3.8.5. Protein blending, adsorption mechanisms and composite reusability

The FTIR analysis indicates that TiO_2@gliadin surface consists of various oxygen containing functional groups formed by hydrophobic and covalent interactions between TiO_2 and gliadin (Fig. 8 (a). Indeed, during gliadin functionalisation, terminal amino acid, carboxyl, hydroxyl (OH) and amines groups protonates or deprotonated and coordinated to O–Ti–O framework covalently or via hydrogen bonding. This resulted in abundant negative charges forming monodentate or bidentate binding sites on TiO_2 vacant oxygen atoms. The additional mechanisms are schemed in supplementary data (Fig. SF 2a). According to zeta potential results, it is possible that certain amino groups of TiO_2@gliadin composite are protonated. However, end-carboxyl groups of amino acids and side groups are ionized especially at alkaline pH likely participated in adsorption of Co^{2+}.

Consequently, hydrogen bonding and hydrophobic interactions, electrostatic and covalent and metallic interactions were among the main mechanisms involved in the adsorption process (Fig. 8b) as early substantiated by isotherm investigations (Mengesha et al., 2022b). The abovementioned mechanisms are extensively clarified in supplementary materials (Fig. SF 2d). The surface area and pore size shown in Table ST3 probably contributed to the improved adsorption capacity. This was further elucidated by thermodynamic assessment. The suggested schematic mechanisms for the removal of Co^{2+} by TiO_2@gliadin are summarised in Fig. 8b.

The composite regeneration highlighted in supplementary data (Text S11) is a crucial step to minimise the environmental impact and the process cost. Several regenerative cycles using 0.5 M HCl as suitable eluent to leach Co^{2+} adsorbed onto TiO_2@gliadin, are shown in supplementary data (Fig. SF 3). Regardless of the affinity and stability of Co^{2+} to form complexes in solution (Mengesha et al., 2022b), the combined acid washing process was effective for the release of Co^{2+} as expected. Fig. 8c shows that TiO_2@gliadin composite maintained its performance even if a slight reduction in adsorption capacity and removal % after five consecutive adsorption cycles was observed with the reused TiO_2@gliadin as compared to the initial composite. This could be ascribed to the fact that active sites on TiO_2@gliadin used were fully occupied by strongly bonded Co^{2+} and co-existing groups. Nevertheless, the 96.5% removal percentage achieved after five cycles still sustains that TiO_2@gliadin composite could successfully be used for industrial applications. The comparative removal of Co^{2+} achieved using various sorbent materials are presented in supplementary materials Table ST9 and discussed in supplementary materials text S13.

4. Conclusions

Metal oxides, TiO_2 and $AgFe_2O_3$ were successfully incorporated into extracted gliadin protein by mechanical and chemical precipitation. SEM-EDS, FTIR, XRD, BET, TGA and zeta potential presented evidence that the dispersion of MOs into gliadin extract likely occurred via hydrophobic, ionic, covalent, electrostatic, hydrogen bonding, resulting in the formation of bidentate chelating and monodentate bridging sites. The highest inhibitory activity of *E. coli* under light and in the dark conditions was observed for TiO_2@gliadin. AgFe–TiO_2@gliadin and $AgFe_2O_3$@gliadin lowered the growth of *E. coli* under the light conditions as compared to the control. The effective retention of Co^{2+} at pH that was varied from 3.5 to 9.5 was observed with TiO_2@gliadin but was more prominent at pH 4 and superior to that of AgFe–TiO_2@gliadin, $AgFe_2O_3$@gliadin, and unmodified gliadin, correspondingly. The adsorption of Co^{2+} onto TiO_2@gliadin best fitted the Langmuir model over Temkin and Freundlich models. The kinetic study indicated that adsorption of Co^{2+} followed the pseudo-second-order kinetic model. The retention of Co^{2+} occurred in three main diffusion stages including external and pore diffusion, and adsorption.

Thermodynamic study showed that the adsorption was an endothermic physisorption process. The used TiO_2@gliadin could be regenerated by washing with 0.5 M HCl and distilled water to retrieve the

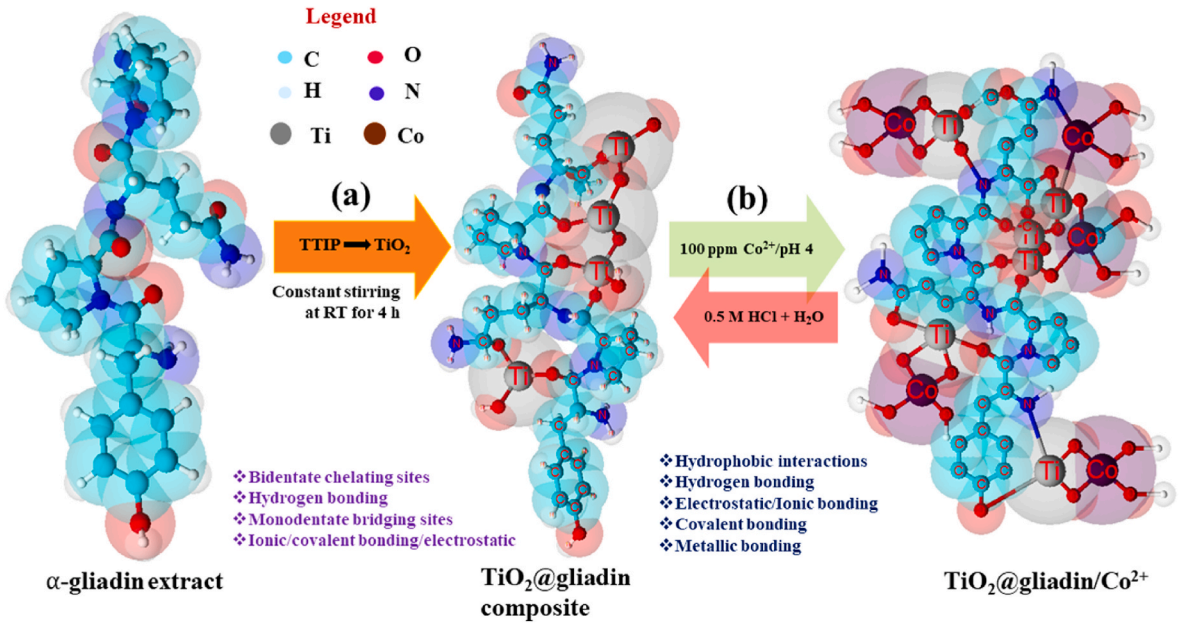

Fig. 8. (a) Possible dispersive blending mechanisms of gliadin by TiO_2 (v:v ratio 1:1, 400 rpm, room temperature, time 4h) and (b) suggested adsorption/desorption mechanisms for the encapsulation of Co^{2+} (C_0 = 100 mg/L, pH = 4, V = 10 mL).

adsorbed Co^{2+}, and the composite could be reused up to five consecutive cycles. The current study demonstrates that gliadin with MOs resulted in novel multifunctional composites with adequate physicochemical, adsorption and bacteria inactivation properties. In the process investigated in this study, the utilization of gliadin in this study presents an environmentally sustainable approach to circular waste management.

Credit authorship contribution

Emile Salomon Massima Mouele (Conceptualisation, Data curation, Writing – original draft), John Kwame Bediako (Review & editing), Youssef El Ouardi (Review & editing), Ikenna Anugwom (Review & editing), Svetlana Butylina (Review & editing), Jean-Luc Mukaba (Review & editing), Leslie. F. Petrik (Review & editing), Myo Tay Zar Myint (Data curation, Review & editing), Htet Htet Kyaw (Data curation, Review & editing), Mohammed Al-Abri (Review & editing), Mohammed A. Al Belushi (Data curation, Review & editing), Sergey Dobretsov (Data curation, Review & editing), Katri Laatikainen (Project administration, review & editing), Eveliina Repo (Supervision, review & editing).

Declaration of competing interest

The authors declare that they have no known competing financial interests or personal relationships that could have appeared to influence the work reported in this paper.

Data availability

Data will be made available on request.

Acknowledgments

The authors would like to thank the South Karelia Säästöpankki Foundation (Finland) for the financial support. The appreciations are also extended to Dr Katri Laatikainen and Prof Eveliina Repo for hosting Dr. Massima at LUT University. In addition, Dr. Bediako expresses profound gratitude for the funding support from the European Union's Horizon 2020 research and innovation program under the Marie Skłodowska-Curie grant agreement No.101026202. This work was also supported by "BATCircle2.0 - Finland-based Circular Ecosystem of Battery Metals (core project 23B350E9YT10)", [grant number 44412/31/2020], Finland.

Appendix A. Supplementary data

Supplementary data to this article can be found online at https://doi.org/10.1016/j.envpol.2023.122788.

To begin with, the accumulation of Co^{2+} in humans could be fatal and often leads to diseases such as rhinitis, allergic dermatitis vasodilation, cardiomyopathy, and asthma. Likewise, the occurrence of *E. coli* bacteria in fresh water often results in infection known as *E. coli* O157 causing stomach pain, diarrhoea, and kidney failure. Gliadin-metal oxides functionalised composites produced in this study are effective for the removal of Co^{2+} and *E. coli* inhibition. Therefore, this approach is green and environmentally friendly for circular waste management and can be applied at both laboratory and industrial scales, making it a favourable alternative for environmental remediation.

I hereby testify that the work covered in this manuscript has not been published or is not under publication elsewhere.

I confirm that we do not have any conflict of interest to disclose. Therefore, I believe that our manuscript is suitable for publication in the journal of "**Environmental Pollution**" under your supervision.

References

Abaee, A., Mohammadian, M., Jafari, S.M., 2017a. Whey and soy protein-based hydrogels and nano-hydrogels as bioactive delivery systems. Trends Food Sci. Technol. 70, 69–81. https://doi.org/10.1016/j.tifs.2017.10.011.

Abaee, A., Mohammadian, M., Jafari, S.M., 2017b. Whey and soy protein-based hydrogels and nano-hydrogels as bioactive delivery systems. Trends Food Sci. Technol. 70, 69–81. https://doi.org/10.1016/j.tifs.2017.10.011.

Alavi, M., Yarani, R., 2022. Nano Micro Biosystems ROS and RNS modulation: the main antimicrobial, anticancer, antidiabetic, and antineurodegenerative mechanisms of metal or metal oxide nanoparticles. Nano Micro Biosystems 2023, 22–30. https://doi.org/10.22034/nmbj.2023.382133.1012.

Amendola, V., Scaramuzza, S., Agnoli, S., Granozzi, G., Meneghetti, M., Campo, G., Bonanni, V., Pineider, F., Sangregorio, C., Ghigna, P., Polizzi, S., Riello, P., Fiameni, S., Nodari, L., 2015. Laser generation of iron-doped silver nanotruffles with magnetic and plasmonic properties. Nano Res. 8, 4007–4023. https://doi.org/10.1007/s12274-015-0903-y.

Antoniou, J., Liu, F., Majeed, H., Qi, J., Yokoyama, W., Zhong, F., 2015. Physicochemical and morphological properties of size-controlled chitosan-tripolyphosphate nanoparticles. Colloids Surf. A Physicochem. Eng. Asp. 465, 137–146. https://doi.org/10.1016/j.colsurfa.2014.10.040.

Atsdr Agency for Toxic Substances and Disease Registry, 2023. ToxFAQs™ for Cobalt. Toxic Substances Portal. https://wwwn.cdc.gov/dcs/ContactUs/Form.
Awual, M.R., Yaita, T., Okamoto, Y., 2014. A novel ligand based dual conjugate adsorbent for cobalt(II) and copper(II) ions capturing from water. Sensor. Actuator. B Chem. 203, 71–80. https://doi.org/10.1016/j.snb.2014.06.088.
Awual, M.R., Yaita, T., Shiwaku, H., Suzuki, S., 2015. A sensitive ligand embedded nano-conjugate adsorbent for effective cobalt(II) ions capturing from contaminated water. Chem. Eng. J. 276, 1–10. https://doi.org/10.1016/j.cej.2015.04.058.
Awual, M.R., Alharthi, N.H., Hasan, M.M., Karim, M.R., Islam, A., Znad, H., Hossain, M. A., Halim, M.E., Rahman, M.M., Khaleque, M.A., 2017. Inorganic-organic based novel nano-conjugate material for effective cobalt(II) ions capturing from wastewater. Chem. Eng. J. 324, 130–139. https://doi.org/10.1016/j.cej.2017.05.026.
Balasubramanian, C., Joseph, B., Gupta, P., Saini, N.L., Mukherjee, S., Di Gioacchino, D., Marcelli, A., 2014. X-ray absorption spectroscopy characterization of iron-oxide nanoparticles synthesized by high temperature plasma processing. J. Electron. Spectrosc. Relat. Phenom. 196, 125–129. https://doi.org/10.1016/j.elspec.2014.02.011.
Beltrame, K.K., Cazetta, A.L., de Souza, P.S.C., Spessato, L., Silva, T.L., Almeida, V.C., 2018. Adsorption of caffeine on mesoporous activated carbon fibers prepared from pineapple plant leaves. Ecotoxicol. Environ. Saf. 147, 64–71. https://doi.org/10.1016/j.ecoenv.2017.08.034.
Borjigin, T., Schmitt, M., Morlet-Savary, F., Xiao, P., Lalevée, J., 2022. Low-cost and recyclable photocatalysts: metal oxide/polymer composites applied in the catalytic breakdown of dyes. Photochemistry 2, 733–751. https://doi.org/10.3390/photochem2030047.
Chen, S., Ma, Y., Dai, L., Liao, W., Zhang, L., Liu, J., Gao, Y., 2021. Fabrication, characterization, stability and re-dispersibility of curcumin-loaded gliadin-rhamnolipid composite nanoparticles using pH-driven method. Food Hydrocolloids 118. https://doi.org/10.1016/j.foodhyd.2021.106758.
Covelo, E.F., Vega, F.A., Andrade, M.L., 2007a. Simultaneous sorption and desorption of Cd, Cr, Cu, Ni, Pb, and Zn in acid soils. I. Selectivity sequences. J. Hazard Mater. 147, 852–861. https://doi.org/10.1016/j.jhazmat.2007.01.123.
Covelo, E.F., Vega, F.A., Andrade, M.L., 2007b. Simultaneous sorption and desorption of Cd, Cr, Cu, Ni, Pb, and Zn in acid soils. I. Selectivity sequences. J. Hazard Mater. 147, 852–861. https://doi.org/10.1016/j.jhazmat.2007.01.123.
Czarnek, K., Terpilowska, S., Siwicki, A.K., 2015. Selected aspects of the action of cobalt ions in the human body. Cent. Eur. J. Immunol. 40, 236–242. https://doi.org/10.5114/ceji.2015.52837.
De Andrade, J.R., Oliveira, M.F., Da Silva, M.G.C., Vieira, M.G.A., 2018. Adsorption of pharmaceuticals from water and wastewater using nonconventional low-cost materials: a review. Ind. Eng. Chem. Res. 57, 3103–3127. https://doi.org/10.1021/acs.iecr.7b05137.
Diseases & Conditions, Coli, E., 2022. Mayo Clinic Minute: Avoiding Summer E. Coli Infection. https://www.mayoclinic.org/diseases-conditions/e-coli/symptoms-causes/syc-20372058. (Accessed 25 August 2023).
Filipcsei, G., Csetneki, I., Szilágyi, A., Zrínyi, M., 2007. Magnetic field-responsive smart polymer composites. Adv. Polym. Sci. 206, 137–189. https://doi.org/10.1007/12_2006_104.
Freitas, C., Mü, R.H., 1998. Effect of Light and Temperature on Zeta Potential and Physical Stability in Solid Lipid Nanoparticle. SLNTM) dispersions.
Gulfam, M., Kim, J.E., Lee, J.M., Ku, B., Chung, B.H., Chung, B.G., 2012. Anticancer drug-loaded gliadin nanoparticles induce apoptosis in breast cancer cells. Langmuir 28, 8216–8223. https://doi.org/10.1021/la300691n.
Health Encyclopedia, 2023. URMC/Encyclopedia/Cobalt, Health Encyclopedia. https://www.urmc.rochester.edu/encyclopedia/content.aspx?contentid=cobalt&contenttypeid=19. (Accessed 25 August 2023).
Hoque, M.S., Benjakul, S., Prodpran, T., 2011. Effects of partial hydrolysis and plasticizer content on the properties of film from cuttlefish (Sepia pharaonis) skin gelatin. Food Hydrocolloids 25, 82–90. https://doi.org/10.1016/J.FOODHYD.2010.05.008.
Jing, N., Tian, M., Wang, Y., Zhang, Y., 2019. Nitrogen-doped carbon dots synthesized from acrylic acid and ethylenediamine for simple and selective determination of cobalt ions in aqueous media. J. Lumin. 206, 169–175. https://doi.org/10.1016/j.jlumin.2018.10.059.
Joye, I.J., Davidov-Pardo, G., Ludescher, R.D., McClements, D.J., 2015a. Fluorescence quenching study of resveratrol binding to zein and gliadin: towards a more rational approach to resveratrol encapsulation using water-insoluble proteins. Food Chem. 185, 261–267. https://doi.org/10.1016/j.foodchem.2015.03.128.
Joye, I.J., Nelis, V.A., McClements, D.J., 2015b. Gliadin-based nanoparticles: fabrication and stability of food-grade colloidal delivery systems. Food Hydrocolloids 44, 86–93. https://doi.org/10.1016/j.foodhyd.2014.09.008.
Kasperiski, F.M., Lima, E.C., Umpierres, C.S., dos Reis, G.S., Thue, P.S., Lima, D.R., Dias, S.L.P., Saucier, C., da Costa, J.B., 2018. Production of porous activated carbons from Caesalpinia ferrea seed pod wastes: highly efficient removal of captopril from aqueous solutions. J. Clean. Prod. 197, 919–929. https://doi.org/10.1016/j.jclepro.2018.06.146.
Kleinfeldt, L., Gädke, J., Biedendieck, R., Krull, R., Garnweitner, G., 2019. Spray-dried hierarchical aggregates of iron oxide nanoparticles and their functionalization for downstream processing in biotechnology. ACS Omega 4, 16300–16308. https://doi.org/10.1021/acsomega.9b01549.
Kostyla, C., Bain, R., Cronk, R., Bartram, J., 2015. Seasonal variation of fecal contamination in drinking water sources in developing countries: a systematic review. Sci. Total Environ. 514, 333–343. https://doi.org/10.1016/j.scitotenv.2015.01.018.
K Y, K., H, K., Sunada, F.A., 1998. Bactericidal and detoxification effects of TiO2 thin film photocatalysts. Environ. Sci. Technol. 32, 726–728.
Liao, L., yue Han, X., ming Zhao, M., Ni, L., bin Liu, Z., Zhang, W., 2016a. Effect of native aggregation state of soluble wheat gluten on deamidation behavior in a carboxylic acid/heat water solution. J. Cereal. Sci. 72, 1–9. https://doi.org/10.1016/j.jcs.2016.09.011.
Liao, L., yue Han, X., ming Zhao, M., Ni, L., bin Liu, Z., Zhang, W., 2016b. Effect of native aggregation state of soluble wheat gluten on deamidation behavior in a carboxylic acid/heat water solution. J. Cereal. Sci. 72, 1–9. https://doi.org/10.1016/j.jcs.2016.09.011.
Y. Liu, ; Hui Xu, J.-H. Tay, Derivation of a General Adsorption Isotherm Model, (n.d.). https://doi.org/10.1061/ASCE0733-93722005131:101466..
Liu, X., Shao, W., Luo, M., Bian, J., Yu, D.G., 2018. Electrospun blank nanocoating for improved sustained release profiles from medicated gliadin nanofibers. Nanomaterials 8. https://doi.org/10.3390/nano8040184.
Lohcharoenkal, W., Wang, L., Chen, Y.C., Rojanasakul, Y., 2014. Protein nanoparticles as drug delivery carriers for cancer therapy. BioMed Res. Int. 2014 https://doi.org/10.1155/2014/180549.
Madhan, B., Subramanian, V., Rao, J.R., Nair, B.U., Ramasami, T., 2005. Stabilization of collagen using plant polyphenol: role of catechin. Int. J. Biol. Macromol. 37, 47–53. https://doi.org/10.1016/j.ijbiomac.2005.08.005.
Majidi, S., Sehrig, F.Z., Farkhani, S.M., Goloujeh, M.S., Akbarzadeh, A., 2016. Current methods for synthesis of magnetic nanoparticles. Artif. Cells, Nanomed. Biotechnol. 44, 722–734. https://doi.org/10.3109/21691401.2014.982802.
Mallakpour, S., Barati, A., 2011. Efficient preparation of hybrid nanocomposite coatings based on poly(vinyl alcohol) and silane coupling agent modified TiO2 nanoparticles. Prog. Org. Coating 71, 391–398. https://doi.org/10.1016/j.porgcoat.2011.04.010.
Marçal, L., De Faria, E.H., Nassar, E.J., Trujillano, R., Martín, N., Vicente, M.A., Rives, V., Gil, A., Korili, S.A., Ciuffi, K.J., 2015. Organically modified saponites: SAXS study of swelling and application in caffeine removal. ACS Appl. Mater. Interfaces 7, 10853–10862. https://doi.org/10.1021/acsami.5b01894.
Mengesha, D.N., Abebe, M.W., Appiah-Ntiamoah, R., Kim, H., 2022a. Ground coffee waste-derived carbon for adsorptive removal of caffeine: effect of surface chemistry and porous structure. Sci. Total Environ. 818. https://doi.org/10.1016/j.scitotenv.2021.151669.
Mengesha, D.N., Abebe, M.W., Appiah-Ntiamoah, R., Kim, H., 2022b. Ground coffee waste-derived carbon for adsorptive removal of caffeine: effect of surface chemistry and porous structure. Sci. Total Environ. 818. https://doi.org/10.1016/j.scitotenv.2021.151669.
M. Moraveji, Impact of Deamidation on the Physicochemical Properties and Air-Water Interfacial Behaviour of Gliadin Nanoparticles, n.d..
Mouele, E.S.M., Dinu, M., Cummings, F., Fatoba, O.O., Myint, M.T.Z., Kyaw, H.H., Parau, A.C., Vladescu, A., Francesconi, M.G., Pescetelli, S., Di Carlo, A., Agresti, A., Al-Abri, M., Dobretsov, S., Braic, M., Petrik, L.F., 2020. Effect of calcination time on the physicochemical properties and photocatalytic performance of carbon and nitrogen co-doped tio2 nanoparticles. Catalysts 10. https://doi.org/10.3390/CATAL10080847.
Nishida, N., Amagasa, S., Kobayashi, Y., Yamada, Y., 2017. Mixture of silver and iron oxide nanoparticles produced by chemical methods. Hyperfine Interact. 238 https://doi.org/10.1007/s10751-017-1445-3.
Odonkor, S.T., Mahami, T., 2020. Escherichia coli as a tool for disease risk assessment of drinking water sources. Internet J. Microbiol. 2020 https://doi.org/10.1155/2020/2534130.
Oleyaei, S.A., Zahedi, Y., Ghanbarzadeh, B., Moayedi, A.A., 2016. Modification of physicochemical and thermal properties of starch films by incorporation of TiO2 nanoparticles. Int. J. Biol. Macromol. 89, 256–264. https://doi.org/10.1016/j.ijbiomac.2016.04.078.
Pereira, R.N., Souza, B.W.S., Cerqueira, M.A., Teixeira, J.A., Vicente, A.A., 2010. Effects of electric fields on protein unfolding and aggregation: influence on edible films formation. Biomacromolecules 11, 2912–2918. https://doi.org/10.1021/bm100681a.
Pongkitdachoti, U., Unob, F., 2018a. Simultaneous adsorption of silver nanoparticles and silver ions on large pore mesoporous silica. J. Environ. Chem. Eng. 6, 596–603. https://doi.org/10.1016/j.jece.2017.12.046.
Pongkitdachoti, U., Unob, F., 2018b. Simultaneous adsorption of silver nanoparticles and silver ions on large pore mesoporous silica. J. Environ. Chem. Eng. 6, 596–603. https://doi.org/10.1016/j.jece.2017.12.046.
Popov, S.V., Markov, P.A., Patova, O.A., Vityazev, F.V., Bakutova, L.A., Borisenkov, M.F., Martinson, E.A., Ananchenko, B.A., Durnev, E.A., Burkov, A.A., Litvinets, S.G., Belyi, V.A., Ipatova, E.A., 2017. In vitro gastrointestinal-resistant pectin hydrogel particles for β-glucuronidase adsorption. J. Biomater. Sci. Polym. Ed. 28, 293–311. https://doi.org/10.1080/09205063.2016.1268461.
Prabhu, S., Poulose, E.K., 2012. Silver nanoparticles: mechanism of antimicrobial action, synthesis, medical applications, and toxicity effects. Int. Nano Lett. 2 https://doi.org/10.1186/2228-5326-2-32.
Qiu, H., Lv, L., Pan, B., Zhang, Q., Zhang, W., Zhang, Q., 2009. Critical review in adsorption kinetic models. J. Zhejiang Univ. - Sci. 10, 716–724. https://doi.org/10.1631/jzus.A0820524.
Sahoo, C., Gupta, A.K., 2015. Characterization and photocatalytic performance evaluation of various metal ion-doped microstructured TiO2 under UV and visible light. J Environ Sci Health A Tox Hazard Subst Environ Eng 50, 659–668. https://doi.org/10.1080/10934529.2015.1011958.
Santoso, E., Ediati, R., Kusumawati, Y., Bahruji, H., Sulistiono, D.O., Prasetyoko, D., 2020. Review on recent advances of carbon based adsorbent for methylene blue removal from waste water. Mater. Today Chem. 16 https://doi.org/10.1016/j.mtchem.2019.100233.

Sapna, D. Kumar, 2018. Biodegradable polymer-based nanoadsorbents for environmental remediation. In: New Polymer Nanocomposites for Environmental Remediation. Elsevier Inc., pp. 261–278. https://doi.org/10.1016/B978-0-12-811033-1.00012-3

Sayed, F.N., Polshettiwar, V., 2015. Facile and sustainable synthesis of shaped iron oxide nanoparticles: effect of iron precursor salts on the shapes of iron oxides. Sci. Rep. 5 https://doi.org/10.1038/srep09733.

Sneharani, A.H., Karakkat, J.V., Singh, S.A., Rao, A.G.A., 2010. Interaction of curcumin with ß-lactoglobulin;stability, spectroscopic analysis, and molecular modeling of the Complex. J. Agric. Food Chem. 58, 11130–11139. https://doi.org/10.1021/jf102826q.

Somchue, W., Sermsri, W., Shiowatana, J., Siripinyanond, A., 2009. Encapsulation of α-tocopherol in protein-based delivery particles. Food Res. Int. 42, 909–914. https://doi.org/10.1016/j.foodres.2009.04.021.

The National Institute for Occupational Safety and Health (NIOSH), 2019. Cobalt. Centers for Disease Control and Prevention. https://www.cdc.gov/niosh/topics/cobalt/default.html. (Accessed 25 August 2023).

Thewissen, B.G., Pauly, A., Celus, I., Brijs, K., Delcour, J.A., 2011. Inhibition of angiotensin I-converting enzyme by wheat gliadin hydrolysates. Food Chem. 127, 1653–1658. https://doi.org/10.1016/j.foodchem.2010.11.171.

Tsai, P.J., She, C.H., 2006. Significance of Phenol−Protein interactions in modifying the antioxidant capacity of peas. J. Agric. Food Chem. 54, 8491–8494. https://doi.org/10.1021/JF061475Y.

Tyagi, A., Tyagi, A., Mir, Z.A., Ali, S., Chaudhary, J., 2020. Nano-materials for wastewater treatment. In: Modern Age Waste Water Problems. Springer International Publishing, pp. 47–67. https://doi.org/10.1007/978-3-030-08283-3_3.

Üstün, E., Önbaş, S.C., Çelik, S.K., Ayvaz, M.Ç., Şahin, N., 2022. Green synthesis of iron oxide nanoparticles by using ficus carica leaf extract and its antioxidant activity. Biointerface Res Appl Chem 12, 2108–2116. https://doi.org/10.33263/BRIAC122.21082116.

Verma, D., Gulati, N., Kaul, S., Mukherjee, S., Nagaich, U., 2018. Protein based nanostructures for drug delivery. J. Pharm. (Lahore). https://doi.org/10.1155/2018/9285854, 2018) 1–18.

Viegas, R.M.C., Campinas, M., Costa, H., Rosa, M.J., 2014. How do the HSDM and Boyd's model compare for estimating intraparticle diffusion coefficients in adsorption processes. Adsorption 20, 737–746. https://doi.org/10.1007/s10450-014-9617-9.

Wanag, A., Rokicka, P., Kusiak-Nejman, E., Kapica-Kozar, J., Wrobel, R.J., Markowska-Szczupak, A., Morawski, A.W., 2018a. Antibacterial properties of TiO2 modified with reduced graphene oxide. Ecotoxicol. Environ. Saf. 147, 788–793. https://doi.org/10.1016/j.ecoenv.2017.09.039.

Wanag, A., Rokicka, P., Kusiak-Nejman, E., Kapica-Kozar, J., Wrobel, R.J., Markowska-Szczupak, A., Morawski, A.W., 2018b. Antibacterial properties of TiO2 modified with reduced graphene oxide. Ecotoxicol. Environ. Saf. 147, 788–793. https://doi.org/10.1016/j.ecoenv.2017.09.039.

Wang, S.Y., Zhu, B.B., Li, D.Z., Fu, X.Z., Shi, L., 2012. Preparation and characterization of TIO 2/SPI composite film. Mater. Lett. 83, 42–45. https://doi.org/10.1016/j.matlet.2012.05.104.

Washington State Department of Health, 2023. Coliform Bacteria in Drinking Water. Washington State Department of Health. https://doh.wa.gov/community-and-environment/drinking-water/contaminants/coliform. (Accessed 25 August 2023).

World Health Organization, E. Coli, World Health Organization, 2018. https://www.who.int/news-room/fact-sheets/detail/e-coli. (Accessed 25 August 2023).

Wu, W., Kong, X., Zhang, C., Hua, Y., Chen, Y., 2018a. Improving the stability of wheat gliadin nanoparticles – effect of gum Arabic addition. Food Hydrocolloids 80, 78–87. https://doi.org/10.1016/j.foodhyd.2018.01.042.

Wu, W., Kong, X., Zhang, C., Hua, Y., Chen, Y., 2018b. Improving the stability of wheat gliadin nanoparticles – effect of gum Arabic addition. Food Hydrocolloids 80, 78–87. https://doi.org/10.1016/j.foodhyd.2018.01.042.

Xu, S., Habib, A.H., Gee, S.H., Hong, Y.K., McHenry, M.E., 2015. Spin orientation, structure, morphology, and magnetic properties of hematite nanoparticles. J. Appl. Phys. 117 https://doi.org/10.1063/1.4914059.

Xue, J., Zhang, Y., Huang, G., Liu, J., Slavin, M., Lucy, L., 2018. Yu, Zein-caseinate composite nanoparticles for bioactive delivery using curcumin as a probe compound. Food Hydrocolloids 83, 25–35. https://doi.org/10.1016/j.foodhyd.2018.04.037.

Yang, S., Dai, L., Sun, C., Gao, Y., 2018. Characterization of curcumin loaded gliadin-lecithin composite nanoparticles fabricated by antisolvent precipitation in different blending sequences. Food Hydrocolloids 85, 185–194. https://doi.org/10.1016/j.foodhyd.2018.07.015.

Yang, S., Liu, L., Chen, H., Wei, Y., Dai, L., Liu, J., Yuan, F., Mao, L., Li, Z., Chen, F., Gao, Y., 2021. Impact of different crosslinking agents on functional properties of curcumin-loaded gliadin-chitosan composite nanoparticles. Food Hydrocolloids 112. https://doi.org/10.1016/j.foodhyd.2020.106258.

Zhang, Y., An, Z., Cui, G., Li, J., 2003a. Stabilized complex film formed by co-adsorption of β-lactoglobulin and phospholipids at liquid/liquid interface. Colloids Surf. A Physicochem. Eng. Asp. 223, 11–16. https://doi.org/10.1016/S0927-7757(03)00099-2.

Zhang, Y., An, Z., Cui, G., Li, J., 2003b. Stabilized complex film formed by co-adsorption of β-lactoglobulin and phospholipids at liquid/liquid interface. Colloids Surf. A Physicochem. Eng. Asp. 223, 11–16. https://doi.org/10.1016/S0927-7757(03)00099-2.

Zhang, Y., Akindolie, M.S., Tian, X., Wu, B., Hu, Q., Jiang, Z., Wang, L., Tao, Y., Cao, B., Qu, J., 2021. Enhanced phosphate scavenging with effective recovery by magnetic porous biochar supported La(OH)3: Kinetics, isotherms, mechanisms and applications for water and real wastewater. Bioresour. Technol. 319 https://doi.org/10.1016/j.biortech.2020.124232.

Zimet, P., Livney, Y.D., 2009. Beta-lactoglobulin and its nanocomplexes with pectin as vehicles for ω-3 polyunsaturated fatty acids. Food Hydrocolloids 23, 1120–1126. https://doi.org/10.1016/j.foodhyd.2008.10.008.

Zolfi, M., Khodaiyan, F., Mousavi, M., Hashemi, M., 2014. Development and characterization of the kefiran-whey protein isolate-TiO2 nanocomposite films. Int. J. Biol. Macromol. 65, 340–345. https://doi.org/10.1016/j.ijbiomac.2014.01.010.